Zircon and quartz inclusions in garnet used for complementary Raman-thermobarometry: application to the Holsnøy eclogite, Bergen Arcs, Western Norway

Xin, Zhong[1], Niels, H., Andersen[2], Marcin, Dabrowski[1,3], Bjørn Jamtveit[1]

1. *Physics of Geological Processes, The Njord Centre, Department of Geosciences, University of Oslo, Norway*
2. *Department of Chemistry, University of Oslo, Norway*
3. *Computational Geology Laboratory, Polish Geological Institute - NRI, Wrocław, Poland*

Corresponding author: Xin Zhong (xinzhong0708@gmail.com)

ABSTRACT

Mineral inclusions are common and have been widely used to investigate complex geological history. When a rock undergoes cooling and decompression after the entrapment of an inclusion into a host mineral, residual pressure may develop within the inclusion because of the differences in thermal expansivity and compressibility between the inclusion and host. By combining laser Raman spectroscopy and experimental data relating hydrostatic pressure and Raman shift, it is possible to estimate the entrapment pressure-temperature (*P-T*) conditions using an isotropic elastic model. In this study, we report Raman spectroscopic data on both zircon and quartz inclusions in garnet host from the Holsnøy eclogite, Bergen Arcs, Norway. Averaged residual pressures based on different Raman peaks for zircon and quartz inclusions are obtained to be ca. 0.6GPa and ca. 0.65GPa respectively. Using the equation of state for zircon and quartz, the entrapment *P-T* conditions are constrained to be 1.7~1.9GPa, 680~760^{o}C, consistent with previous estimates based on phase equilibria. Heating/cooling experiments are performed on an entrapped zircon inclusion. A clear trend is found between the residual zircon inclusion pressure and the externally controlled temperature. We show that the residual zircon inclusion pressure sealed in garnet host is very sensitive to the entrapment temperature, and can be used as a Raman-thermometer. The effects of laser heating and the thermo-elastic anisotropy of zircon inclusion are quantified and discussed.

INTRODUCTION

The determination of pressure and temperature (*P-T*) history for metamorphic rocks is a crucial ingredient in metamorphic petrology. Most endeavours in recovering the metamorphic *P-T* history are undertaken via phase equilibria and thermobarometry techniques that are based on equilibrium thermodynamics (see e.g. Berman, 1988; Spear, 1995; Connolly, 2005; Anderson, 2005; De Capitani and Petrakakis, 2010; Holland and Powell, 2011). An alternative method that has recently received substantial attention is based on the mechanical equilibrium between entrapped mineral inclusions (e.g. quartz) and host mineral (e.g. garnet). Due to the differences of compressibility and thermal expansivity between inclusion and host, residual pressure may develop within the inclusion as confining pressure and temperature change (e.g. Rosenfeld and Chase, 1961; Zhang, 1998). Laser Raman spectroscopy has been applied to obtain the spectral shifts of the entrapped mineral inclusions in a thin-section. The measured spectral shifts can be converted to residual inclusion pressures using experimental calibrations, e.g. quartz data in Liu and Mernagh (1992), or Schmidt and Ziemann (2000). By applying a 1D elastic model for spherical, elastically isotropic inclusions, the entrapment *P-T* conditions can be recovered (Rosenfeld and Chase, 1961; Gillet et al., 1984; Zhang, 1998; Guiraud and Powell, 2006; Angel et al., 2014). For example, the quartz-in-garnet system has been often used for Raman-barometry owing to the large difference in compressibility between quartz and garnet (Enami et al. 2007; Kouketsu et al. 2014; Angel et al. 2015; Taguchi et al. 2016; Bayet et al. 2018). Experiments were performed on natural and synthetic

quartz-in-garnet systems to confirm the validity and precision of quartz-in-garnet Raman-barometry (Ashley et al. 2016; Thomas and Spear 2018). The effect of elastic anisotropy of quartz inclusion on the Raman shift was discussed in Murri et al. (2018). Apart from the most commonly studied quartz-in-garnet system, apatite-in-garnet Raman-barometry has been successfully applied to skarns (Ashley et al. 2017; Barkoff et al. 2018). Feldspar inclusions in different host crystals have been tested to provide thermobarometric constraints in magmatic rocks (Befus et al. 2018).

When applying the Raman thermobarometry technique, many factors may affect the recovered entrapment P-T conditions. As many entrapped inclusions are not perfectly spherical, a correction factor was introduced by Mazzucchelli et al. (2018) to take into account the effect of various mineral inclusion shapes. Another factor that may influence the residual pressure is the presence of stress-free thin-section surfaces. The significance of stress relaxation due to the finite thickness of thin-section has been investigated experimentally in Campomenosi et al. (2018) and mathematically in Zhong et al. (2018a). Even if the inclusions are close to spherical and fully entrapped in thin-section, lower than expected residual pressure has been reported in e.g. Korsakov et al. (2009), which may be related to the viscous creep of garnet host at high temperature conditions. This effect has been investigated in Zhong et al. (2018b) to quantify the amount of pressure relaxation due to viscous creep of the host garnet, which cannot be directly measured with Raman spectroscopy. These factors point to an issue that although Raman-thermobarometry is useful, it needs to be performed with cautions.

In this contribution, we report Raman spectroscopic data of quartz and zircon inclusions in garnets from an eclogite sample from the Holsnøy Island, Bergen Arcs, Western Norway. Zircon has a slightly higher bulk modulus (ca. 200GPa, Van Westrenen et al. 2004) than garnet (ca. 170GPa, Bass, 1995), but it has a significantly lower thermal expansion coefficient than garnet (only ca. the half of garnet, see Özkan 2008; Fei, 1995). This property makes zircon an ideal candidate for Raman-thermometry because high-residual inclusion pressure is expected after cooling from the entrapment temperature to room temperature (e.g. see Kohn, 2014). Here, we demonstrate with Raman spectroscopic measurements and elastic modelling that zircon inclusions in garnet host are suitable for Raman-thermometry. We also demonstrate that quartz and zircon inclusions entrapped in garnet crystals in the same thin-section provide complementary thermo-barometric constraints on the entrapment metamorphic conditions, which are consistent with previous estimates using other phase equilibria technique. Heating/cooling experiments were also performed to verify zircon-in-garnet Raman-thermometry and this demonstrates the robustness of the method. Finally, the effect of thermo-elastic anisotropy of zircon inclusions on the residual strain and stress components were modelled and discussed. The level of laser power applied to zircon inclusions was systematically varied to investigate the effect of local heating that may cause variations on the spectral shift.

SAMPLE DESCRIPTIONS

The studied eclogite sample is from Holsnøy Island that belongs to Lindås Nappe in Bergen arc, south-west Norway (60°36'32.00''N, 05°05'45.60''E). The protolith was a mangeritic, 930 Ma old, granulite from Landsvik that was subsequently buried and transformed into eclogite during the Caledonian Orogeny at ca. 425-430 Ma (Austrheim and Griffin 1985; Jamtveit et al. 2018a). Previous *P-T* estimates for the formation of eclogite were in the range 1.5~2.1GPa, 650~800°C (Austrheim, 1987; Austrheim and Griffin, 1985; Jamtveit et al., 1990; Pollok et al., 2008, Bhowany et al., 2018). The process of eclogitization from granulite facies is considered to be driven by the influx of externally derived fluids (Austrheim, 1987; Jamtveit et al., 1990, 2000; Jackson et al., 2004). The observations of pseudotachylyte veins and associated wall rock fragmentation have been taken to indicate that fluid introduction was linked to deep earthquakes (Austrheim 2013; Austrheim et al. 2017; Jamtveit et al. 2018b; Petley-Ragan et al. 2018).

Microphotographs of the studied sample HA10-90 are shown in Fig. 1, where garnet, rutile, amphibole and apatite crystals can be found. Zoisite has been seen in the neighbouring sample HA11-90. Amphibole forms large crystals or fill in garnet as veins (Fig. 1). Apatite often exists as large inclusions in garnet with at least 20μm size. For the 30μm thick thin-section in this study, these apatite inclusions are often exposed at thin-section surface or bottom. Therefore, their residual pressures have been substantially relaxed. Quartz inclusions are often found in garnet mantle and rim, while zircon are randomly distributed in the entire thin-section. Clusters of zircon

122 inclusions are observed as shown in Fig. 1. Zircon inclusions that are too close to each
123 other (within 1~2 radius) are avoided. Both quartz and zircon inclusions are identified
124 and measured with Raman spectroscopy. The size of analysed inclusions is mostly in
125 between 2 and 8μm. Most analysed inclusions are completely entrapped in the
126 thin-section with >5μm distance from the thin-section surface/bottom. When
127 searching for inclusions, the objective was typically placed in the middle of the
128 thin-section to avoid inclusions close to sample edges. Meanwhile, reflected light was
129 used to check for full entrapment before every measurement.

130 **METHODS**

131 **Analytical methods**

132 We used a Horiba Jobin-Yvon (T64000) Raman spectrograph located at the
133 Department of Chemistry at the University of Oslo. The entrance slit width was 100
134 microns and the grating was 900 lines pr. mm. With a spectrograph focal length of 64
135 cm and a 1024x256 open electrode CCD with 2.56-by-2.56 µm sized pixels we
136 achieved a spectral width of 5.1cm^{-1}. The spectral range from 115 to 1470cm^{-1} allows
137 for simultaneous observation of two gas-discharge lamp Neon emission lines for
138 calibration (540.056 and 576.442nm appearing at ca. 276.4 and 1445.5 cm^{-1},
139 respectively). All collected Raman spectra have been aligned following the Neon peak
140 at ca. 276.4cm^{-1}. The sum of Gaussian-Lorentzian equation was used to fit the Raman
141 spectra with the MATLAB "*lsqcurvefit*" function. The baseline was corrected by
142 adding a single variable to the Gaussian-Lorentzian sum-function. Spectral windows

were carefully chosen to include each Raman peak when executing the MATLAB code. We double checked the automatic fit result for each selected Raman peak of all the inclusions visually to avoid erroneous results. Based on the fitting function, the uncertainties of the spectral shifts can be obtained, which vary depending on the widths and intensities of the Raman bands. For zircon, the uncertainty (derived from the MATLAB function) of 1008cm^{-1} band is the lowest (<0.03 cm^{-1}) and the uncertainties of the rest bands are within 0.15cm^{-1}. For quartz, the 464 and 128 cm^{-1} Raman bands have an uncertainty ca. 0.1cm^{-1}, while the 206cm^{-1} band has an uncertainty higher than 0.2cm^{-1}.

It is possible that the fitted Raman band positions are convolved with the tails of the neighbouring bands, e.g. the quartz 206cm^{-1} band with garnet bands at ca. 210~220 cm^{-1}. For zircon, most Raman bands are very sharp and the spectral windows for fitting are carefully chosen to minimize the systematic error. In this study, the convolution effect on fitted spectral shift is considered to be minor.

The laser for the Raman instrument was a Spectra-Physics diode pumped Nd: YVO4 Millennia Pro SJ12 model yielding 200mW power at 532.1nm. A set of three neutral density (ND) filters was used for damping the laser power (individual damping percentages were 90%, 50% and 33%, respectively). The Raman spectra were calibrated with pure 4-Acetamidophenol powder every a few hours to monitor the spectral scale variation during a day. Good analytical reproducibility was obtained every day (standard deviation is ca. 0.3cm^{-1}), implying that the laser and the Raman instrument is very stable. When testing the effect of laser power on Raman shifts of a

particular zircon inclusion, all possible combinations of the three ND filters were applied. The laser power has been measured directly beneath the 50x objectives with a laser power meter model 407A from Spectra-Physics. The measured laser power at the sample surface, covered the range from ca. 2 to 72 mW.

Heating/cooling experiments have been performed using a thermostated aluminium box specially designed for temperature control (inner dimensions 50x30x5 mm). Two small off-axis tubes (7mm outer diameter) connected to both ends of the box allow a flow of dry nitrogen through the cell and ensured good thermal contact with the sample. Through the outlet tube, a type K thermocouple was inserted with the lead welding-point just above the thin-section surface. The sample box was kept above the microscope stage to avoid thermal conduction. Round cover-glasses (0.15mm thick BK7 glass) ca. 15mm in diameter served as optical windows on both sides of the sample box that allow for search for mineral inclusions within the transparent glass-covered area. A slight flow of dry air was blown over the top window to prevent icing, and the whole box was thermally insulated with black 4mm thick Armaflex tape (Ahlsell AB). The nitrogen entrance tube was fixed to the outlet of an Oxford Instruments Flow cryostat. The achieved stable temperature range was between ca. -150 ~ 100^{o}C.

The chemical composition of garnet was studied using a Hitachi SU5000 FE-SEM (Schottky FEG) scanning electron microscopy (SEM) with a Dual Bruker XFlash30 Energy Dispersive X-ray Spectroscopy (EDS) system located at Department of Geosciences, University of Oslo. SEM/EDS were performed on carbon coated thin

187 sections under high vacuum with 15 kV current. Copper stubs coated with Au were
188 used to mount the sample in the vacuum chamber.

189 **Zircon residual pressure calculations**

190 Seven Raman peaks for zircon inclusions are clearly observed with wavenumbers 202,
191 214, 224, 356, 439, 975 and 1008cm^{-1} (Fig. 2). The zircon peak at 356cm^{-1} is
192 significantly interfered by a garnet peak at ca. 220cm^{-1}. In spite of that, it is clear that
193 the 356cm^{-1} peak shifts towards higher wavenumber when *P* increases (see Fig. 2).
194 Four zircon peaks with wavenumbers at around 202, 439, 975 and 1008cm^{-1} were
195 used in this study. The 214 and 224cm^{-1} peaks are both wider than the 202cm^{-1} peak,
196 and often a partial overlap of these occur (see Fig. 2). They are also close to the garnet
197 peak at ca. 210~220cm^{-1}. The 202cm^{-1} peak shows slight negative shift towards
198 higher pressure (Schmidt et al. 2013). Therefore, it further increases its spectral
199 distance to all the other peaks for high pressure inclusions. This is an advantage that
200 may reduce the errors for the conversion of Raman shift to residual pressure. Hence,
201 we define three parameters to obtain the residual zircon inclusion pressure as follows:

$$\begin{aligned} \Delta\omega_1 &= \bar{\nu}_{1008} - \bar{\nu}_{202} \\ \Delta\omega_2 &= \bar{\nu}_{975} - \bar{\nu}_{202} \\ \Delta\omega_3 &= \bar{\nu}_{439} - \bar{\nu}_{202} \end{aligned} \quad (1)$$

202 where $\bar{\nu}_{1008}$ is the measured wavenumber of the 1008cm^{-1} peak. An unstrained gem
203 quality zircon crystal is measured at its surface as standard. The measurements were
204 performed at three sub-perpendicular orientations at the surface of the crystal to

obtain the Raman shift for relaxed zircon at room *P-T* conditions. The fitted Raman peaks originating from different zircon orientations are very consistent and within an error range of less than 0.2cm^{-1}. These peaks have been averaged to be the zircon standard.

Three independent residual zircon inclusion pressures can be calculated using the defined three parameters:

$$P_1 = \frac{\Delta\omega_1^{inc} - \Delta\omega_1^{relax}}{5.77+0.45}$$
$$P_2 = \frac{\Delta\omega_2^{inc} - \Delta\omega_2^{relax}}{5.16+0.45} \quad (2)$$
$$P_3 = \frac{\Delta\omega_3^{inc} - \Delta\omega_3^{relax}}{1.45+0.45}$$

where $\Delta\omega_1^{relax}$ is for the relaxed single zircon crystal (standard) and $\Delta\omega_1^{inc}$ is for zircon inclusions. The pressure unit is GPa. The derivatives of the Raman shift with respect to pressure is based on Schmidt et al. (2013). The derivatives are: 5.77cm^{-1}/GPa for 1008cm^{-1} band, 5.16cm^{-1}/GPa for 975cm^{-1} band, 1.45cm^{-1}/GPa for 439cm^{-1} band, and -0.45cm^{-1}/GPa for 202cm^{-1} band.

Isotropic elastic model

We used an isotropic elastic model to predict the residual zircon/quartz inclusion pressure and to recover the entrapment *P-T* conditions (Guiraud and Powell 2006). The model assumes that both the inclusion and host are elastically isotropic. The 1D elastic model gives:

$$P_{inc} = \frac{4G}{3}\left(\frac{V_{inc}^{25^oC,P_{inc}}}{V_{inc}^{T_{etp},P_{etp}}} - \frac{V_{host}^{25^oC,1bar}}{V_{host}^{T_{etp},P_{etp}}}\right) \quad (3)$$

where P_{inc} is the residual pressure for either zircon or quartz inclusion, G is the garnet shear modulus, $V_{inc}^{25^oC,P_{inc}}$ is the specific volume of inclusion at room temperature and residual pressure, $V_{inc}^{T_{etp},P_{etp}}$ is the inclusion specific volume at entrapment *P-T* conditions, and $V_{host}^{25^oC,1bar}$ is the garnet host specific volume at room *P-T* condition. An iterative solver has been used to obtain P_{inc}. The almandine, grossular and pyrope PVT relationships are based on Milani et al. (2015) and spessartine is fitted based on the PVT data of Gréaux and Yamada (2014) with the EoSFit7c program (Angel et al. 2014a). Third-order Birch-Murnaghan equation of state (EoS) and thermal pressure are applied (Holland and Powell 2011). The quartz EoS is based on Angel et al. (2017) (fully curved EoS).

RESULTS

Residual inclusion pressure

Over 100 zircon inclusions and 36 quartz inclusions from over 20 garnet grains have been analysed for sample HA10-90 from the Holsnøy Island, Bergen Arcs, Norway. The results are shown in Fig. 3 and Fig. 4. Round zircon inclusions were preferred when searching for the inclusions. The laser beam is focused at the centre of the inclusions. Apart from fully entrapped inclusions, some exposed inclusions were analysed as well. These typically contain very low residual pressure (red diamond markers in Fig. 3 and Fig. 4). For zircon inclusions, the pressures calculated based on

240 the two parameters $\Delta\omega_1$ and $\Delta\omega_2$ are very consistent. A high-density cluster of
241 highly pressurized zircon inclusions is present at ca. 0.6GPa. There are some fully
242 entrapped zircon inclusions containing less than ~0.5GPa residual pressure. It is
243 speculated that a small proportion of the measured inclusions may potentially contain
244 microcracks to partially relax the pressure that cannot be observed directly via
245 microscopy. An average zircon pressure of ~0.57GPa was obtained from these
246 relaxed zircon inclusions, and those with less than ~0.3GPa were not considered. The
247 pressure determined based on $\Delta\omega_3$ was less consistent compared to the two other
248 estimates, presumably due to the fact that the 439cm^{-1} Raman band is less sensitive to
249 pressure changes (1.45cm^{-1}/GPa).

250 It is noted that four outliers with pressures of ca. 0.8GPa are observed (magenta dots).
251 These outlier inclusions are relatively round as observed at the thin-section plane but
252 with averaged diameters smaller than 2~3 μm. It is possible that stress concentration
253 occurs at the inclusion rim (potentially in the vertical direction that is difficult to
254 observe under microscope), and is captured by the finite-sized laser beam spot.
255 Although the laser spot has an apparent 1-by-1 μm size at the thin-section plane, its
256 effective size in the vertical dimension is at least two times larger than 1μm and
257 complicated to estimate accurately. An increased risk of convolution effects along the
258 Z-axis may potentially lead to some degree of increase in Raman shift due to the
259 stress concentration at the inclusion rim/corner. It has been reported that over 25%
260 pressure (Raman shift) increase can be present at the entrapped quartz inclusion rim

(Murri et al. 2018), which is on the same level as observed for the outliers in this study.

About 36 quartz inclusions have been found in sample HA10-90. The residual pressures were estimated via the Raman bands at wavenumbers 128, 206 and 464cm^{-1}. A fully unstrained, euhedral, transparent quartz crystal ca. 6cm long was used as the quartz-standard. The experimental data from Schmidt and Ziemann (2000) was applied to recover the pressure based on the Raman shift (for the 128cm^{-1} band the calibration curve was fitted by Thomas and Spear (2018): $P_{128} = 0.13143\Delta\bar{\nu}_{128} + 0.00475\Delta\bar{\nu}_{128}^2$, where $\Delta\bar{\nu}_{128}$ is the shift of 128cm^{-1} peak relative to the standard quartz measured at room *P-T* conditions). The residual pressures obtained using the 128 and 464cm^{-1} peaks were very consistent. However, the 206cm^{-1} band yields a slightly lower pressure estimate. It is likely that the 206cm^{-1} band is interfered by the garnet peak at around 210~220cm^{-1} (Ashley et al. 2015). The maximal quartz inclusion pressure obtained is ca. 0.65GPa (ca. 5μm size inclusion). However, due to the limited number of quartz inclusions and the absence of a high residual pressure cluster, we do not rule out the possibility that quartz inclusions with even higher pressures potentially may be present in the rock. Here, we chose 0.65GPa as the maximal quartz inclusion pressure for the purpose of recovering the entrapment pressure.

Zircon and quartz Raman-thermobarometry

The elasticity and thermal expansion coefficients of zircon have been reported in previous studies: e.g. Austin (1931); Bayer (1972); Subbarao et al. (1990); Bass (1995); Finch (2003); Van Westrenen et al. (2004) and Özkan (2008) etc. Here, we fit the bulk modulus (K_0) and its derivative with respect to pressure (K') using the measurements of synthetic pure zircon from Van Westrenen et al. (2004). The thermal expansion coefficient (α_{V0}) and its derivative with respect to temperature ($\frac{\partial \alpha_V}{\partial T}$) were estimated based on the data from Austin (1931). The constant $\frac{\partial K}{\partial T}$ was obtained from the *ab initio* calculations of Chiker et al. (2016). The other constant $\frac{\partial \alpha_V}{\partial P}$ was obtained via the Maxwell relationship. These parameters are given in Table 1. The calculated PVT relationship is shown in Fig. 4. Using the isotropic elastic model in Eq. 3 and the afore-mentioned EoS of garnet endmembers, we show the calculated residual zircon inclusion pressure isopleths in Fig. 5. The residual pressures for four different garnet endmember hosts were fitted with polynomial functions in Fig. 5 for future geological applications.

Among the four endmember hosts, it is found that the zircon-in-almandine system yields the lowest residual pressure, while the zircon-in-pyrope system yields the highest residual pressure. Grossular and spessartine hosts provide intermediate and similar residual inclusion pressure. Here, the volume is averaged based on the molar fraction of different endmembers in a garnet mixture (Milani et al. 2015). The results are shown in Fig. 6. The effect of garnet composition on the predicted entrapment temperature is rather large. For the endmember case with either pure almandine or

302 pure pyrope, the difference of inferred entrapment temperature may reach ca. 200ºC
303 given 1GPa entrapment pressure. This is due to the distinct thermal expansion
304 coefficient between these almandine and pyrope endmembers (see e.g. Fei, 1995).
305 The almandine-to-pyrope ratio relevant for the eclogitization conditions in Holsnøy
306 eclogite estimated by Bhowany et al. (2018) is highlighted with light blue shading.

307 For sample HA10-90, the garnet composition is ca. $Alm_{0.45\text{-}0.65}Prp_{0.20\text{-}0.40}Grs_{0.14}Sps_{0.01}$
308 as shown in Fig. 6B. Using the measured quartz inclusion pressure (ca. 0.65GPa) and
309 zircon inclusion pressure (ca. 0.6GPa), complementary Raman thermobarometry is
310 performed. The garnet composition is defined as the garnet core, ca.
311 $Alm_{0.45}Prp_{0.40}Grs_{0.14}Sps_{0.01}$, where most zircon inclusions were found (see Fig. 6B).
312 As shown in Fig. 7, thermometric and barometric constraints are obtained that cross at
313 temperature range 680~760ºC (average ca. 720ºC) and pressure range 1.7~1.9GPa
314 (averaged ca. 1.8GPa). These estimates were compared to the constructed clockwise
315 *P-T* path in Bhowany et al. (2018) , and the peak eclogitization conditions in Jamtveit
316 et al. 1990) and Raimbourg et al. (2007). Four stages of eclogitization have been
317 introduced in Bhowany et al. (2018) as shown by the yellow stars. The peak
318 eclogitization *P-T* conditions from Jamtveit et al. (1990) and Raimbourg et al. (2007)
319 are shown by the pink and green boxes in Fig. 7, respectively.

320 It is noted that the measured garnet core composition in sample HA10-90
321 ($Alm_{0.45}Prp_{0.40}Grs_{0.14}Sps_{0.01}$) lies between the garnet core composition reported for
322 stage 3 and stage 4 from Bhowany et al. (2018) (stage 3:
323 $Alm_{0.45\text{-}0.46}Prp_{0.29\text{-}0.30}Grs_{0.22\text{-}0.28}Sps_{0.01}$ and stage 4:

$Alm_{0.30-0.38}Prp_{0.45-0.46}Grs_{0.15-0.16}Sps_{0.01}$). It is closer to the composition reported in stage 4. Based on Bhowany et al. (2018), stage 3 of eclogitization corresponds to *P-T* range of 670~690°C, 2.1~2.2GPa and stage 4 corresponds to *P-T* range of 680~700°C, 1.6~1.7GPa (see Fig. 7). Therefore, both our *P-T* constraints and the garnet composition fall between the estimates of stage 3 and stage 4 of eclogitization. Meanwhile, our thermal estimate (ca. 680~760°C) is rather consistent with Raimbourg et al. (2007) (around 720°C), and slightly higher than Jamtveit et al. (1990) (660~720°C). The determined entrapment pressure based on quartz-in-garnet Raman-barometry is slightly lower than previous estimate by ca. 0.3GPa. It is possible that viscous relaxation may have slightly relax the residual quartz inclusion pressure, which is mainly developed during the isothermal decompression process (Zhong et al. 2018b).

Heating and cooling test of zircon residual pressure

Although the elastic model has shown that zircon can be applied for Raman-thermometry, additional experimental heating/cooling tests are performed here to confirm that residual zircon pressure can be substantially influenced by the controlled temperature on the stage. The purpose here is not to precisely determine the slope of the residual inclusion pressure with respect to temperature using experimental method, but to verify the significance of temperature and quantify the uncertainty of zircon-in-garnet Raman-thermometry. Silicon is first investigated as a test run to verify the thermal setup in the experiment. The results are shown in Fig. 8. The theoretical calculations for Raman shift based on Cowley (1965) and the

experimental measurements from Hart et al. (1970) are shown and compared to our measurements. The results are very consistent to the predictions from both theoretical calculations and experimental measurements.

Subsequently, a fully entrapped and near-spherical high-pressure (ca. 0.6GPa at room condition) zircon inclusion in crack-free garnet is used to perform heating/cooling test. After varying the stage temperature by ca. 200°C (from ca. -110 to 90°C), it is clear that a trend of residual zircon inclusion pressure is present (Fig. 9).

It is known that both temperature and pressure changes may lead to the (volumetric) strains, which cause the variation of spectral shift. The Raman shift is in fact directly related to strains instead of pressure and temperature (Angel et al. 2018; Murri et al. 2018). In order to obtain the residual pressure at various temperature conditions, the effect of temperature on spectral shift (strains) must be subtracted from the measure shift (strains). Therefore, the residual pressure is computed following the equation below:

$$P_{inc}(T) = \frac{\bar{\nu}_{1008}^{measure} - \bar{\nu}_{1008}^{T}}{5.77} \quad (4)$$

where $\bar{\nu}_{1008}^{measure}$ is the measured Raman shift of 1008cm^{-1} band, $\bar{\nu}_{1008}^{T}$ is the expected Raman shift solely due to the controlled temperature (T) at room pressure. Here, it is considered that cross term ($\bar{\nu}_{PT}$) is zero.

The effect of temperature on Raman shift at room pressure is as follows based on Schmidt et al. (2013).

$$\bar{\nu}_{1008}^{T} = 7.54 \cdot 10^{-9}T^3 - 1.61 \cdot 10^{-5}T^2 - 2.89 \cdot 10^{-2}T + 1008.75 \quad (5)$$

where T is the stage temperature in ^{o}C. After each temperature change, the system is held for ca. 15mins to reach thermal equilibrium before measurement. Our measured standard zircon Raman shift at room *P-T* conditions is about 1008.02cm^{-1}. Therefore, the last coefficient (1008.75) has been slightly varied from 1008.9cm^{-1} as reported in Schmidt et al. (2013) to match our zircon standard measured at room temperature condition. Such small difference may be caused by different Raman machine/laser settings or calibration protocols.

The measured Raman shift $\bar{\nu}_{1008}^{measure}$ and the computed $\bar{\nu}_{1008}^{T}$ are substituted into Eq. 4 to obtain the residual pressure (see Table 2). It is shown in Table 2 that the difference between the measured Raman shift and the expected Raman shift solely due to temperature change increases towards lower stage temperature. This is due to the residual zircon pressure increase as temperature drops, which causes additional Raman shift ($\bar{\nu}_{1008}^{P} = \bar{\nu}_{1008}^{measure} - \bar{\nu}_{1008}^{T}$).

An elastic model is also performed to compare its results with measurements. For this studied zircon inclusion, the entrapment *P-T* conditions are estimated to ca. 1.8GPa, 700^{o}C (pressure based on quartz inclusion barometry). The stage (final) temperature is changed from room temperature to values between -150 to 150^{o}C with the entrapment *P-T* unchanged (see Eq. 3). The residual inclusion pressure at different stage temperature can thus be calculated.

The fitted slope of the measured residual zircon inclusion pressure as a function of stage temperature is ca. -0.00078(35) GPa/°C. The slope based on the elastic model is ca. -0.00103 GPa/°C (for temperatures higher than -120°C). It is shown that the slope based on the experiment is lower than theoretically modelled. However, the modelled slope (-0.00103 GPa/°C) is within the 1σ-range of the measured slope (-0.00043 to -0.00113 GPa/°C). The latter large uncertainty arises because the range of stage temperatures (ca. 200°C) is not sufficiently large to ensure significant inclusion pressure variation. However, the observed trend clearly confirms the sensitivity of residual zircon inclusion pressure to temperature changes.

Effect of laser power on Raman shift

Zircon can be opaque and may absorb the laser energy causing a local heating effect. This may potentially alter the temperature of a zircon inclusion during measurement, and lead to an artificially induced thermal expansion and hence alter the Raman shift. Here, we applied different laser powers to a high-pressure zircon inclusion by combining three different filters, which individually reduce the incident laser power by 90%, 50% and 33%, respectively. The residence time was about 30s which is sufficient for Raman measurement. Subsequently, the same laser filter combination was applied to a selected zircon inclusion to obtain the Raman shift as a function of laser power.

It is shown in Fig. 10 that a laser power of less than ca. 10mW is safe regarding the risk of inducing a Raman shift. When the laser power surpassed a power of ca. 20mW,

405 the measured Raman shift of the 1008cm^{-1} band dramatically decreased, most likely
406 due to local heating that reduces the peak wavenumber (Schmidt et al. 2013). Then a
407 clear trend of Raman shift as a function of applied laser power was observed. Up to ca.
408 2cm^{-1} decrease was observed when the laser power came close to 100mW. Assuming
409 that pressure is not changed due to local thermal variation, this shift would correspond
410 to a ~60°C temperature increase based on Eq. 5. However, as thermal expansion due
411 to laser heating may cause additional stress build-up (this would increase the Raman
412 shift further), the actual temperature might be much higher than 60°C to compensate
413 for the local thermal expansion effect within zircon. A similar Raman shift caused by
414 laser power variation has also been confirmed for rutile (TiO_2) (Zhang et al. 2013).

415 It is shown here also, that even for short residence time measurements, the laser
416 power must be carefully chosen to avoid heating the zircon inclusions. In this study,
417 we typically applied laser powers lower than 3~5mW to eliminate the above
418 mentioned heating effect. However, it should be noted that the garnet host also may
419 absorb part of the laser energy, thus our estimate may only provide an upper bound
420 for the safe laser power, although the studied zircon inclusion was very shallow (only
421 ca. 3~4μm from the thin-section surface).

422 **DISCUSSION**

423 **Applicability of zircon-in-garnet Raman thermometry**

424 As natural zircon contains trace amounts of radioactive elements such as U and Th, its
425 phonon frequencies may be influenced by the structural damage due to the radioactive

426 decay of these elements. The metamictization of zircon has been investigated in e.g.
427 Nasdala et al. (1995) and Zhang et al. (2000). The effect of radioactive decay on
428 zircon Raman spectra is shown in Fig. 11b based on the measurements in Zhang et al.
429 (2000). Their results demonstrate a continuous decrease of the phonon frequencies
430 (wavenumber) and an increase of full-width at half-maximum (FWHM) with
431 increasing radiation dose. However, no obvious relation has been found in our data
432 between the FWHM of 1008cm^{-1} peak and its Raman shift ($\Delta\omega_1$) (Fig. 11). This is
433 consistent with the results reported in Binvignat et al. (2018) that zircon pressure
434 within 2.5GPa does not significantly change the FWHM until the atomic
435 rearrangements happen at pressure 2.5GPa (also at 6.5GPa).

436 Therefore, it is considered that the measured systematic Raman shift is dominated by
437 residual zircon inclusion pressure because of: 1) the minor variation of the FWHM
438 with standard deviation ca. 0.45cm^{-1}; 2) the vague influence of residual zircon
439 pressure (Raman shift $\Delta\omega_1$) on FWHM as shown in Fig. 11; and 3) the resemblance
440 of the Raman spectra shape between our measurement and the natural zircon applied
441 with low radioactive dosage that produce little/no change on phonon frequencies (Fig.
442 11 and Zhang et al., 2000); 4) the consistent estimates of residual zircon inclusion
443 pressures based on the three independent parameters ($\Delta\omega_1$, $\Delta\omega_2$ and $\Delta\omega_3$) that
444 involve four different zircon Raman peaks; 5) the experimentally confirmed trend in
445 Fig. 9 which shows that residual zircon inclusion pressure increases as stage
446 temperature decreases.

447 In this work, we have used the bulk modulus of a pure synthetic zircon crystal
448 (ZrSiO4) from Van Westrenen et al. (2004). The reported bulk modulus is ca. 199GPa,
449 which is considerably lower than that of Özkan and Jamieson (1978), where
450 nonmetamict zircon yields a bulk modulus ca. 228GPa. This may lead to some
451 variations on the predition of entrapment *P-T* conditions.

452 **Thermo-elastic anisotropy of zircon inclusion**

453 One major source of uncertainty for zircon-in-garnet Raman-thermometry is the
454 thermo-elastic anisotropy of zircon inclusion. After cooling and decompression, the
455 stress and strain may not be isotropic. It has been confirmed that the Raman shift is
456 controlled by individual strain components rather than the pressure, temperature or
457 volumetric strain (Angel et al. 2018; Murri et al. 2018). For highly anisotropic zircon,
458 the relationship between Raman shift and individual strain components has been
459 recently determined by Stangarone et al. (2019). The thermal expansivity and stiffness
460 tensor of zircon at high *P-T* conditions are not available. Therefore, we assume
461 thermo-elastic isotropy in this study for zircon-in-garnet Raman-thermometry and
462 neglect the fact that zircon is highly anisotropy in its elasticity and thermal
463 expansivity (see e.g. Bass, 1995; Fei, 1995).

464 In order to demonstrate the significance of thermo-elastic anisotropy on the residual
465 stress and strain state of zircon inclusion in garnet, we apply the classical Eshelby's
466 solution and the equivalent eigenstrain method (Eshelby 1957) assuming constant
467 thermo-elasticity within the *P-T* space as given in Table 3. A brief introduction to the

Eshelby's solution and equivalent eigenstrain method are provided in the Appendix (see also Mura 1987). The isotropic elastic model in Eq. 3 is also applied for comparison. For the isotropic elastic model, the PVT relationship is exactly the same as in the anisotropic model.

It is demonstrated that the residual differential stress and differential strain based on the anisotropic model can be quite high, ca. 0.4GPa and 0.02 for eclogite and granulite facies rocks respectively (Fig. 12). However, the pressure is similar to the prediction from the isotropic model. The difference in pressure between the anisotropic model and the isotropic model is less than 0.03GPa for most geologically relevant entrapment *P-T* conditions. Nevertheless, as the Raman shift is controlled by individual strain components rather than hydrostatic pressure, the contribution due to differential strain (stress) may not be small (Stangarone et al. 2019). For the studied Holsnøy eclogite (700ºC, 1.8GPa), the residual differential stress is ca. 0.25~0.3GPa and the residual strain is about 0.0015. The effect of residual differential strain/stress on zircon-in-garnet Raman-thermometry is not covered in this study, and requires further investigations (e.g. the complete stiffness tensor/thermal expansivity at high *P-T* conditions). The recovered entrapment *P-T* conditions in this study can also be refined provided more complete experimental data will become available.

Although it is possible to compute the residual stress/strain of zircon inclusion in garnet host after exhumation, it is noted that inconsistent elasticity data for zircon exist in literature. For example, the used elasticity in this work is based on Özkan and Jamieson (1978): $C_{11} = 424.4$, $C_{12} = 69.2$, $C_{13} = 150.2$ and $C_{33} = 489.6$ (see

Table 3). However, based on the elasticity data summarized in Bass (1995), the zircon's stiffness tensor is: $C_{11} = 256$, $C_{12} = 175$, $C_{13} = 214$ and $C_{33} = 372$. Although the averaged bulk moduli are similar, the elastic anisotropy is significantly different between individual data.

Geological implications

Raman spectroscopy is a simple and inexpensive experimental tool in geological applications. Apart from using Raman to distinguish between different minerals, the spectral shifts provide unique information on the strain/stress state preserved in mineral inclusions. By using a simple elastic model, it is possible to extract stress/strain information measured by Raman spectroscopy to inversely recover *P*-*T* conditions from when the inclusions were entrapped. In this work, we have demonstrated that quartz and zircon inclusions can be successfully applied to obtain *P* and *T* constraints, respectively.

Zircon is a very common accessory mineral found in igneous rocks, metamorphic rocks and detrital grains in sedimentary rocks. Apart from geochronology, the application of zircon for Raman-thermometry may have a great future potential in constraining the conditions of formation for relevant rocks. The application of zircon inclusions in garnet host for Raman thermometry may serve as an unique tool to investigate rocks for which temperature is difficult to constrain by other methods.

Zircon usually contains a non-negligible amount of Hf, which may affect the Raman spectral positions. It has been reported that the up to 10cm^{-1} spectral variation in the

511 1008cm^{-1} peak can be assigned to such variations in composition; from pure zircon
512 ($ZrSiO_4$) to hafnon ($HfSiO_4$), and the trend between spectral shift and Hf/(Zr+Hf) is
513 linear (Grüneberger et al. 2016). As natural zircon commonly do not contain Hf more
514 than 5~10%, the effect of Hf on the spectral shift is considered to be minor (less than
515 1cm^{-1}). In this study, the Hf content of zircon from Holsnøy eclogite is in between
516 0.5~1.5wt% (Bingen et al. 2004), and our unstrained zircon standard is measured to
517 be ~1.7wt% with electron microprobe. Therefore, the effect of Hf on the Raman
518 spectral shift is considered to be minor (<0.01cm^{-1}) in our work.

519 **CONCLUSIONS**

520 In this study, we obtained Raman spectroscopic measurements on zircon and quartz
521 inclusions in garnet from an eclogite sample of Holsnøy Island, Bergen Arcs, Norway.
522 Systematic investigations involving Raman spectroscopy, numerical modelling and
523 heat/cooling experiments confirmed that the zircon-in-garnet system can be applied
524 for Raman-thermometry. Combined with quartz-in-garnet Raman-barometry, we
525 obtained both pressure and temperature constraints on the studied eclogite sample.
526 The recovered eclogitization *P-T* conditions are 680~760^{o}C and 1.7~1.9GPa, broadly
527 consistent with previous estimates based on phase equilibria. Using an anisotropic
528 elastic model based on the classical Eshelby's solution and the equivalent eigenstrain
529 method, we found that high differential stress/strain exist for zircon inclusions
530 recovered from high entrapment *P-T* conditions. It has been shown that differential
531 stress may reach ca. 0.4GPa for eclogite/granulite facies. However, pressures

calculated with anisotropic and isotropic model are rather consistent with each other. When measuring the Raman shift of zircon inclusion, care must be taken to set the laser power to less than 10mW (for 30s laser acquisition time) to avoid local heating effects. Otherwise, the local heating on zircon inclusion may cause a reduction of Raman spectral shift as observed in this study. We suggest that zircon-in-garnet system can be used for potential Raman-thermometry studies that provide complementary results with more commonly applied quartz-in-garnet Raman-barometry.

ACKNOWLEDGEMENTS

H. Austrheim is acknowledged for providing the thin-section samples. S. Simonsen is thanked for her technical support with SEM/EDS. XZ thanks S. Cionoiu, H. Wang and J. Szczepański for helpful discussions. This project has been supported by the Early-Postdoc Mobility Fellowship of Swiss National Science Foundation (SNSF) (P2EZP2_172220) to XZ, and the European Union's Horizon 2020 Research and Innovation Programme under the ERC Advanced Grant Agreement n°669972, 'Disequilibrium Metamorphism' ('DIME') to BJ. MD acknowledges PGI-NRI project no. 61-9015-1601-00-0. We thank D. Rubatto for editorial work and two anonymous reviewers for their helpful comments.

REFERENCES

Anderson G (2005) Thermodynamics of natural systems. Cambridge University Press

552 Angel RJ, Alvaro M, Miletich R, Nestola F (2017) A simple and generalised P–T–V
553 EoS for continuous phase transitions, implemented in EosFit and applied to
554 quartz. Contrib to Mineral Petrol 172:1–15

555 Angel RJ, Gonzalez-Platas J, Alvaro M (2014a) EosFit7c and a Fortran module
556 (library) for equation of state calculations. Zeitschrift fur Krist 229:405–419

557 Angel RJ, Mazzucchelli ML, Alvaro M, et al (2014b) Geobarometry from
558 host-inclusion systems: The role of elastic relaxation. Am Mineral 99:2146–2149

559 Angel RJ, Murri M, Mihailova B, Alvaro M (2018) Stress, strain and Raman shifts.
560 Zeitschrift für Krist 234:129–140

561 Angel RJ, Nimis P, Mazzucchelli ML, et al (2015) How large are departures from
562 lithostatic pressure? Constraints from host–inclusion elasticity. J Metamorph
563 Geol 33:801–813

564 Ashley KT, Barkoff DW, Steele-macinnis M (2017) Barometric constraints based on
565 apatite inclusions in garnet. Am Mineral 102:743–749

566 Ashley KT, Darling RS, Bodnar RJ, Law RD (2015) Significance of "stretched"
567 mineral inclusions for reconstructing P–T exhumation history. Contrib to
568 Mineral Petrol 169:1–9

569 Ashley KT, Steele-MacInnis M, Bodnar RJ, Darling RS (2016) Quartz-in-garnet
570 inclusion barometry under fire: Reducing uncertainty from model estimates.
571 Geology 44:699–702

572 Austin JB (1931) The thermal expansion of some refractory oxides. J Am Ceram Soc
573 14:795–810

574 Austrheim H (1987) Eclogitization of lower crustal granulites by fluid migration
575 through shear zones. Earth Planet Sci Lett 81:221–232

576 Austrheim H (2013) Fluid and deformation induced metamorphic processes around
577 Moho beneath continent collision zones: Examples from the exposed root zone
578 of the Caledonian mountain belt, W-Norway. Tectonophysics 609:620–635

579 Austrheim H, Dunkel KG, Plümper O, Ildefonse B (2017) Fragmentation of wall rock
580 garnets during deep crustal earthquakes. Sci Adv 3:1–8

581 Austrheim H, Griffin WL (1985) Shear deformation and eclogite formation within
582 granulite-facies anorthosites of the Bergen Arcs, western Norway. Chem Geol
583 50:267–281

584 Barkoff DW, Ashley KT, Steele-macinnis M (2018) Pressures of skarn mineralization
585 at Casting Copper , Nevada , USA , based on apatite inclusions in garnet.
586 Geology 1:947–950

587 Bass JD (1995) Elasticity of Minerals, Glasses, and Melts. In: Mineral Physics &
588 Crystallography: A Handbook of Physical Constants. pp 45–63

589 Bayer G (1972) Thermal expansion of ABO4-compounds with zircon- and scheelite
590 structures. J Less-Common Met 26:255–262

591 Bayet L, John T, Agard P, et al (2018) Massive sediment accretion at ~ 80 km depth
592 along the subduction interface : Evidence from the southern Chinese Tianshan.
593 Geology 46:495–498

594 Befus KS, Lin JF, Cisneros M, Fu S (2018) Feldspar Raman shift and application as a
595 magmatic thermobarometer. Am Mineral 103:600–609

596 Berman RG (1988) Internally consistent thermodynamic data for minerals in the
597 system Na2O-K2O-CaO-MgO-FeO-Fe2O-SiO2-TiO2-H2O-CO2. J Petrol
598 29:445–552

599 Bhowany K, Hand M, Clark C, et al (2018) Phase equilibria modelling constraints on
600 P–T conditions during fluid catalysed conversion of granulite to eclogite in the
601 Bergen Arcs, Norway. J Metamorph Geol 36:315–342

602 Bingen B, Austrheim H, Whitehouse MJ, Davis WJ (2004) Trace element signature
603 and U-Pb geochronology of eclogite-facies zircon, Bergen Arcs, Caledonides of
604 W Norway. Contrib to Mineral Petrol 147:671–683

605 Binvignat FAP, Malcherek T, Angel RJ, et al (2018) Radiation-damaged zircon under
606 high pressures. Phys Chem Miner 45:981–993

607 Campomenosi N, Mazzucchelli ML, Mihailova BD, et al (2018) How geometry and
608 anisotropy affect residual strain in host inclusion system: coupling experimental
609 and numerical approaches. Am Mineral 103:2032–2035

610 Chiker F, Boukabrine F, Khachai H, et al (2016) Investigating the Structural, Thermal,
611 and Electronic Properties of the Zircon-Type ZrSiO4, ZrGeO4 and HfSiO4
612 Compounds. J Electron Mater 45:5811–5821

613 Connolly JAD (2005) Computation of phase equilibria by linear programming: A tool
614 for geodynamic modeling and its application to subduction zone decarbonation.
615 Earth Planet Sci Lett 236:524–541

616 Cowley RA (1965) Raman scattering from crystals of the diamond structure. J Phys
617 26:659–667

618 De Capitani C, Petrakakis K (2010) The computation of equilibrium assemblage
619 diagrams with Theriak/Domino software. Am Mineral 95:1006–1016

620 Enami M, Nishiyama T, Mouri T (2007) Laser Raman microspectrometry of
621 metamorphic quartz: A simple method for comparison of metamorphic pressures.
622 Am Mineral 92:1303–1315

623 Eshelby JD (1957) The determination of the elastic field of an ellipsoidal inclusion,
624 and related problems. In: Proceedings of the Royal Society of London A:
625 Mathematical, Physical and Engineering Sciences. The Royal Society, pp 376–
626 396

627 Fei Y (1995) Thermal Expansion. In: Mineral Physics and Crystallography: A
628 handbook of physical constants. pp 29–44

629 Finch RJ (2003) Structure and Chemistry of Zircon and Zircon-Group Minerals. Rev
630 Mineral Geochemistry 53:1–25

631 Gillet P, Ingrin J, Chopin C (1984) Coesite in subducted continental crust : P - T
632 history deduced from an elastic model. Earth Planet Sci Lett 70:426–436

633 Gréaux S, Yamada A (2014) P-V-T equation of state of Mn3Al2Si3O12 spessartine
634 garnet. Phys Chem Miner 41:141–149

635 Grüneberger AM, Schmidt C, Jahn S, et al (2016) Interpretation of Raman spectra of
636 the zircon–hafnon solid solution. Eur J Mineral 28:721–733

637 Guiraud M, Powell R (2006) P-V-T relationships and mineral equilibria in inclusions
638 in minerals. Earth Planet Sci Lett 244:683–694

639 Hart TR, Aggarwal RL, Lax.B. (1970) Temperature dependence of Raman scattering
640 in silicon. Phys Rev B 1:638

641 Holland TJB, Powell R (2011) An improved and extended internally consistent
642 thermodynamic dataset for phases of petrological interest, involving a new
643 equation of state for solids. J Metamorph Geol 29:333–383

644 Jackson JA, Austrheim H, McKenzie D, Priestley K (2004) Metastability, mechanical
645 strength, and the support of mountain belts. Geology 32:625–628

646 Jamtveit B, Austrheim H, Malthe-Sørenssen a (2000) Accelerated hydration of the
647 Earth's deep crust induced by stress perturbations. Nature 408:75–78

Jamtveit B, Ben-Zion Y, Renard F, Austrheim H (2018a) Earthquake-induced transformation of the lower crust. Nature 556:487–491

Jamtveit B, Bucher-Nurminen K, Austrheim H (1990) Fluid controlled eclogitization of granulites in deep crustal shear zones, Bergen arcs, Western Norway. Contrib to Mineral Petrol 104:184–193

Jamtveit B, Moulas E, Andersen TB, et al (2018b) High Pressure Metamorphism Caused by Fluid Induced Weakening of Deep Continental Crust. Sci Rep 8:17011

Kohn MJ (2014) "Thermoba-Raman-try": Calibration of spectroscopic barometers and thermometers for mineral inclusions. Earth Planet Sci Lett 388:187–196

Kolesov BA, Geiger CA (1998) Raman spectra of silicate garnets. Phys Chem Miner 25:142–151

Korsakov A V., Perrakim M, Zhukov VP, et al (2009) Is quartz a potential indicator of ultrahigh-pressure metamorphism ? Laser Raman spectroscopy of quartz inclusions in ultrahigh-pressure garnets. Eur J Mineral 21:1313–1323

Kouketsu Y, Nishiyama T, Ikeda T, Eniami M (2014) Evaluation of residual pressure in an inclusion – host system using negative frequency shift of quartz Raman spectra. Am Mineral 99:433–442

Liu L, Mernagh TP (1992) High Pressure Raman study of the a-quartz forms of SiO2 and GeO2 at room temperature. High Temp Press 24:13–21

668 Mazzucchelli ML, Burnley P, Angel RJ, et al (2018) Elastic geothermobarometry:
669 Corrections for the geometry of the host-inclusion system. Geology 1–4

670 Milani S, Nestola F, Alvaro M, et al (2015) Diamond-garnet geobarometry: The role
671 of garnet compressibility and expansivity. Lithos 227:140–147

672 Mura T (1987) Micromechanics of Defects in Solids. Springer Science & Business
673 Media

674 Murri M, Mazzucchelli ML, Campomenosi N, et al (2018) Raman elastic
675 geobarometry for anisotropic mineral inclusions. Am Mineral

676 Nasdala L, Irmer G, Wolf D (1995) The degree of metamictization in zircon: a Raman
677 spectroscopic study. Eur. J. Mineral. 7:471–478

678 Ono S, Tange Y, Katayama I, Kikegawa T (2004) Equations of state of ZrSiO4
679 phases in the upper mantle. Am Mineral 89:185–188

680 Özkan H (2008) Correlations of the temperature and pressure dependencies of the
681 elastic constants of zircon. J Eur Ceram Soc 28:3091–3095

682 Özkan H, Jamieson JC (1978) Pressure dependence of the elastic constants of
683 nonmetamict zircon. Phys Chem Miner 224:215–224

684 Petley-Ragan A, Dunkel KG, Austrheim H, et al (2018) Microstructural Records of
685 Earthquakes in the Lower Crust and Associated Fluid-Driven Metamorphism in
686 Plagioclase-Rich Granulites. J Geophys Res Solid Earth 123:3729–3746

687 Pollok K, Lloyd GE, Austrheim H, Putnis A (2008) Complex replacement patterns in
688 garnets from Bergen Arcs eclogites: A combined EBSD and analytical TEM
689 study. Chemie der Erde - Geochemistry 68:177–191

690 Raimbourg H, Goffé B, Jolivet L (2007) Garnet reequilibration and growth in the
691 eclogite facies and geodynamical evolution near peak metamorphic conditions.
692 Contrib to Mineral Petrol 153:1–28

693 Rosenfeld JL, Chase AB (1961) Pressure and temperature of crystallization from
694 elastic effects around solid inclusions in minerals? Am. J. Sci. 259:519–541

695 Schmidt C, Steele-MacInnis M, Watenphul A, Wilke M (2013) Calibration of zircon
696 as a Raman spectroscopic pressure sensor to high temperatures and application to
697 water-silicate melt systems. Am Mineral 98:643–650

698 Schmidt C, Ziemann MA (2000) In situ Raman spectroscopy of quartz: A pressure
699 sensor for hydrothermal diamond-anvil cell experiments at elevated temperatures.
700 Am Mineral 85:1725–1734

701 Spear FS (1995) Metamorphic Phase Equilibria And
702 Presure-Temperature-Time-Paths. Mineralogical Society of America

703 Stangarone C, Angel RJ, Prencipe M, et al (2019) Measurement of strains in zircon
704 inclusions by Raman spectroscopy. Eur J Mineral

705 Subbarao EC, Agrawal DK, McKinstry HA, et al (1990) Thermal Expansion of
706 Compounds of Zircon Structure. J Am Ceram Soc 73:1246–1252

707 Subbarao EC, Gokhale KVGK (1968) Thermal Expansion of Zircon. Jpn J Appl Phys
708 1126

709 Taguchi T, Enami M, Kouketsu Y (2016) Prograde evolution of Sulu UHP
710 metamorphic rock in Yangzhuang, Junan region, deduced by combined Raman
711 and petrological studies. J Metamorph Geol 34:683–696

712 Thomas JB, Spear FS (2018) Experimental study of quartz inclusions in garnet at
713 pressures up to 3.0 GPa: evaluating validity of the quartz-in-garnet inclusion
714 elastic thermobarometer. Contrib to Mineral Petrol 173:1–14

715 Van Westrenen W, Frank MR, Hanchar JM, et al (2004) In situ determination of the
716 compressibility of synthetic pure zircon (ZrSiO4) and the onset of the
717 zircon-reidite phase transition. Am Mineral 89:197–203

718 Zhang M, Salje EKH, Farnan I, et al (2000) Metamictization of zircon: Raman
719 spectroscopic study. J Phys Condens Matter 12:1915–1925

720 Zhang Y (1998) Mechanical and phase equilibria in inclusion-host systems. Earth
721 Planet Sci Lett 157:209–222

722 Zhang Y, Harris CX, Wallenmeyer P, et al (2013) Asymmetric lattice vibrational
723 characteristics of rutile TiO2as revealed by laser power dependent raman
724 spectroscopy. J Phys Chem C 117:24015–24022

725 Zhong X, Dabrowski M, Jamtveit B (2018a) Analytical solution for the stress field in
726 elastic half space with a spherical pressurized cavity or inclusion containing
727 eigenstrain. Geophys J Int 216:1100–1115

728 Zhong X, Moulas E, Tajčmanová L (2018b) Tiny timekeepers witnessing high-rate
729 exhumation processes. Sci Rep 8:2234

730

731

732 **FIGURE**

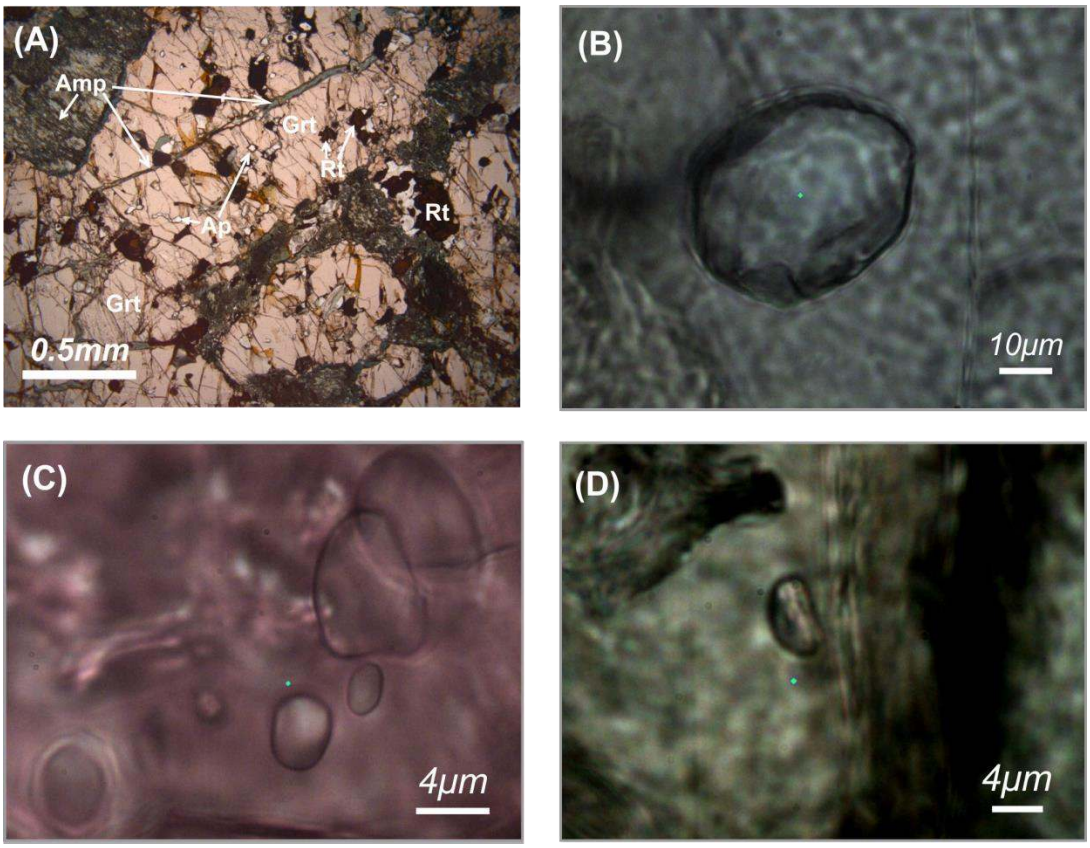

733

734 Fig. 1. (A) shows a microphotograph of sample HA10-90 from Holsnøy Island.
735 Garnet, amphibole, apatite, rutile are observed. Garnet takes ca. 80% volume of the
736 thin-section, amphibole and opaque rutile fill in most of the space between garnet
737 grains. Amphibole veins are observed cross-cutting the garnet grain. Apatite crystals
738 are found as inclusions in garnet. (B), (C) and (D) illustrate apatite, zircon and quartz
739 inclusions, respectively. Most apatite inclusions are larger than 20μm, thus are
740 exposed like in (A) (thin-section is 30μm thick). Zircon inclusions are relatively
741 round and typically form clusters like in (C). Smaller zircon inclusions, e.g. at the
742 center often possess larger residual pressure than the larger ones, e.g. at top right.

743

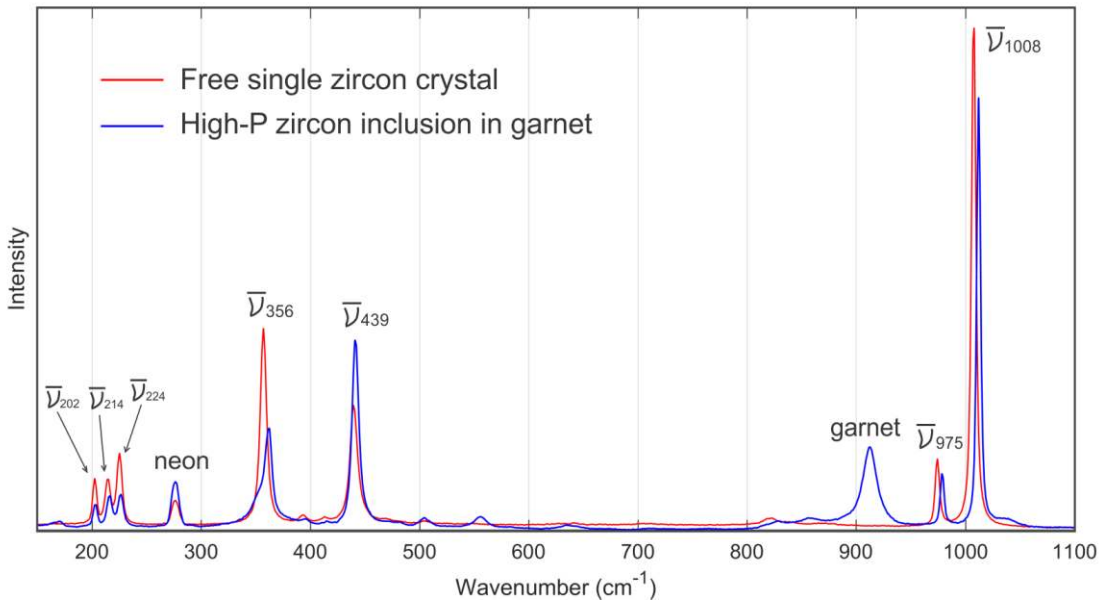

744

745 Fig. 2. Raman spectra containing several zircon peaks at wavenumbers around 202,
746 214, 224, 356, 439, 975 and 1008cm^{-1}. Neon light (ca. 275cm^{-1}) is used for internal
747 calibration. Zircon peak at 356cm^{-1} can be clearly observed but is significantly
748 interfered by the garnet peak, thus it is not used in this work. The zircon peaks at 214
749 and 224cm^{-1} often partially overlap with each other and can be interfered by garnet
750 peak at 210~220cm^{-1}. The visible garnet peaks are around 350, 500, 560, 870, 920
751 and 1040cm^{-1} (Kolesov and Geiger 1998). It is shown that the wavenumbers of the
752 Raman peaks at 356, 975 and 1008cm^{-1} all increase significantly for high pressure
753 inclusion. The positive shift of 439cm^{-1} peak is less significant compared to the other
754 pressure sensitive peaks as its pressure derivative is only 1.45cm^{-1}/GPa (5.77cm^{-1}/GPa
755 for 1008cm^{-1} peak, 5.16cm^{-1}/GPa for 975cm^{-1} peak, 4.56cm^{-1}/GPa for 356cm^{-1} peak).
756 The low-wavenumber zircon peaks at 202, 214, 224cm^{-1} shift only slightly even if
757 pressure is high.

758

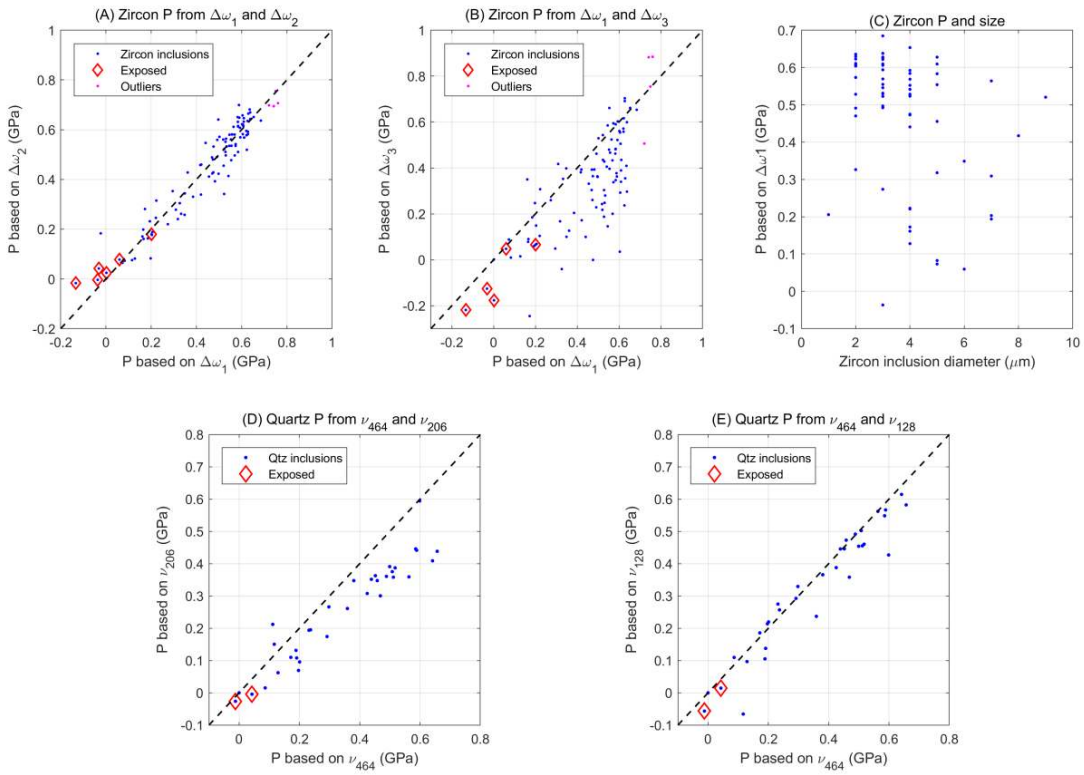

759

760 Fig. 3. (A-B) Zircon inclusion pressure based on the parameter combinations
761 $\Delta\omega_1, \Delta\omega_2$ and $\Delta\omega_1, \Delta\omega_3$, respectively (Eq. 1 and 2). Red diamond markers indicate
762 the inclusions that are exposed at thin-section surface. At ca. 0.6GPa, a high-density
763 cluster is observed, potentially reflecting the peak entrapment temperature condition.
764 (C) Zircon pressure with respective to inclusion diameter (rounded to integer). No
765 clear correlation between inclusion size and residual pressure is found. (D-E) Quartz
766 inclusion pressures converted from Raman spectroscopic data. In (D), the 206cm^{-1}
767 band yields slightly lower estimate of pressure, potentially due to the interference
768 from garnet at similar frequency. The maximal quartz pressure is ca. 0.65GPa based
769 on 128 and 464 cm^{-1} Raman bands.

770

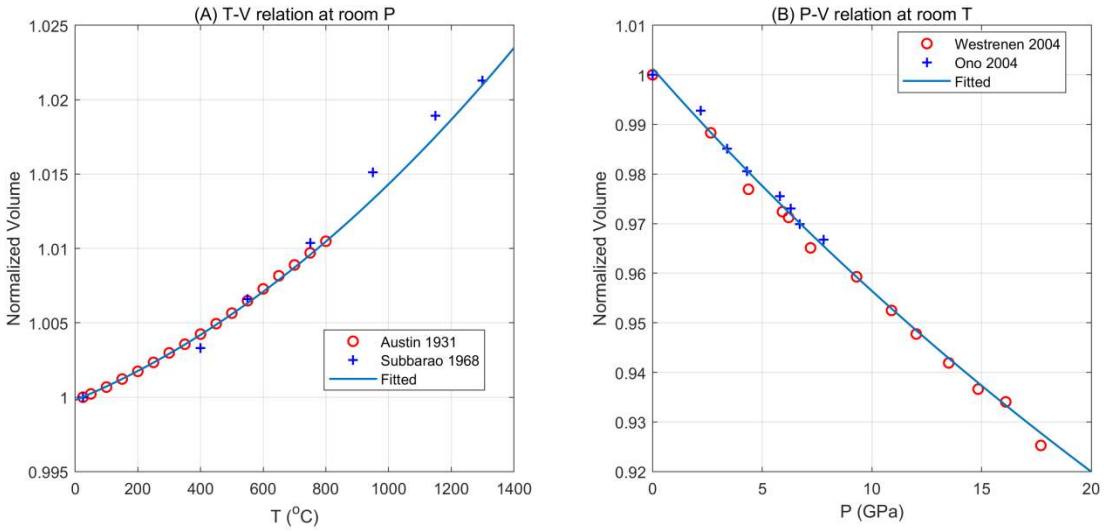

Fig. 4. Experimental and fitted P-V-T data of zircon. (A) shows the T-V relation at room P measured by Austin (1931) and Subbarao and Gokhale (1968). (B) shows the P-V relation at room T measured by Van Westrenen et al. (2004) and Ono et al. (2004). Fitting is performed using the data from Austin (1931) (below 800°C) and Van Westrenen et al. (2004). The fitted thermal expansion and bulk modulus are provided in Table 1 (linear $\frac{\partial K}{\partial T}$ model) for computing the volume.

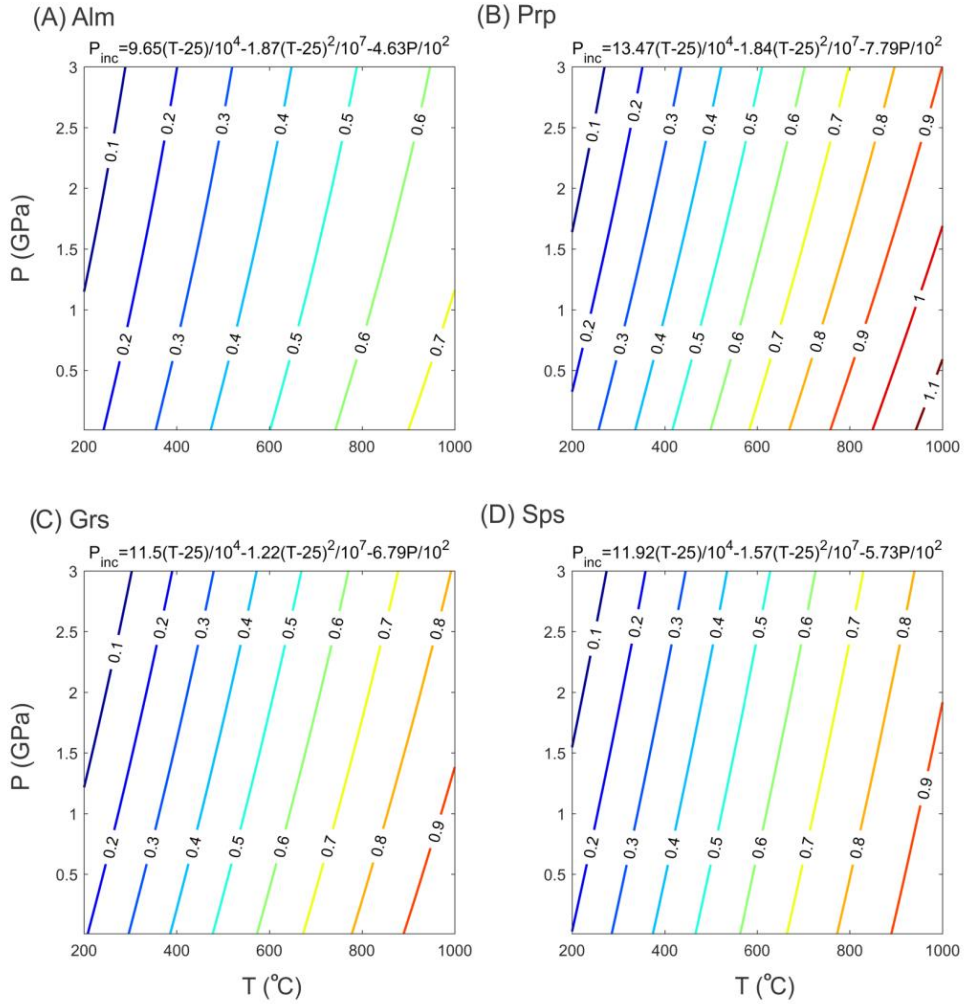

781

782 Fig. 5. Calculated zircon inclusion pressure isomekes for different garnet endmembers.
783 Zircon EoS in Table 1 is used. The EoS of almandine, grossular and pyrope are based
784 on Milani et al. (2015) and spessartine is fitted based on the PVT data of Gréaux and
785 Yamada (2014) with EoSFit7c program (Angel et al. 2014a). Third-order
786 Birch-Murnaghan EoS and thermal pressure are applied (Holland and Powell 2011).
787 Regression is applied to obtain the residual zircon inclusion pressure as functions of
788 entrapment *P-T* conditions. The uncertainty for the regressed zircon pressure is
789 <0.01GPa. The pressure unit is GPa and temperature unit is °C.

790

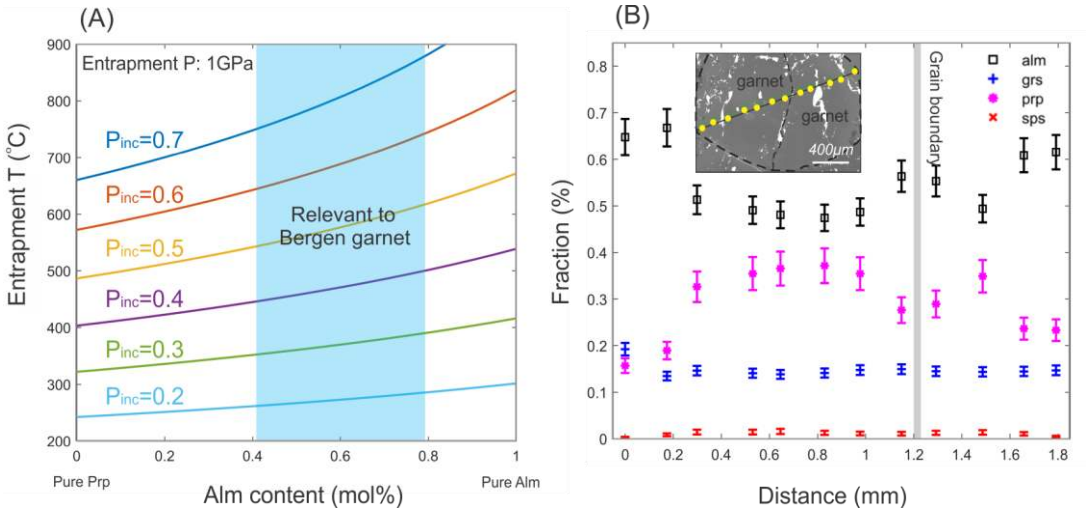

Fig. 6. (A) Entrapment temperature as a function of almandine composition in alm-prp mixture. The specific volume of garnet is averaged based on molar fraction. The curves show entrapment temperature at different residual zircon inclusion pressures. The entrapment pressure is fixed at 1GPa. It is shown that the alm-prp ratio may pose significant influence on entrapment temperature, up to ca. 200°C in extreme case of pure endmember. (B) Endmember molar fractions of two "annealed" garnet crystals ca. 1mm size each in sample HA10-90. Almandine is enriched at the garnet rim and pyrope is enriched at the garnet core. Grossular and spessartine are relatively homogeneous. The yellow dots on garnet denote the measurement points.

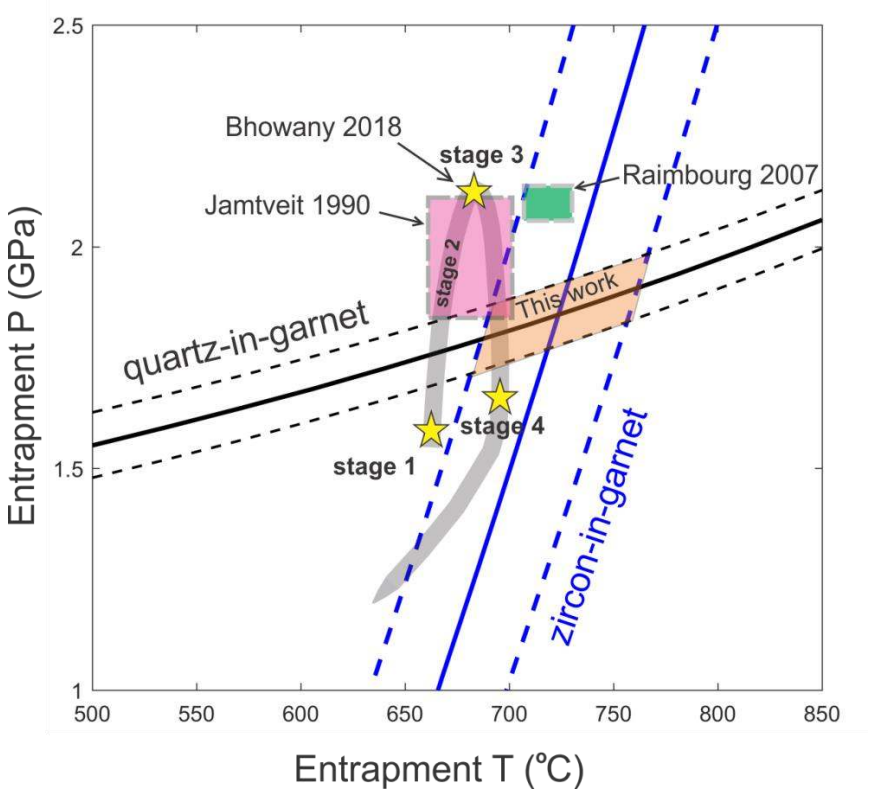

802

803 Fig. 7. Zircon-in-garnet thermometry (blue contours) and quartz-in-garnet barometry
804 (black contours) results for the Holsnøy Island eclogite. Our constrained T range is
805 680~760°C and P range is 1.7~1.9GPa. The *P-T* path based on Bhowany et al. (2018)
806 is illustrated with grey curve. The *P-T* conditions of eclogitization based on Jamtveit
807 et al. (1990) and Raimbourg et al. (2007) are shown with the pink and green boxes,
808 respectively. In this study the temperature is slightly higher than the maximal
809 temperature estimated ca. 700°C in Bhowany et al. (2018) (grey curve) and Jamtveit
810 et al. (1990). The uncertainties in Raman-thermobarometry results are obtained based
811 on an uncertainty of 0.2cm^{-1} Raman spectral shift propagated to residual inclusion
812 pressure. The garnet core composition is taken as $Alm_{0.45}Prp_{0.40}Grs_{0.14}Sps_{0.01}$, which is
813 in between the garnet composition observed between stage 3 and stage 4 (Bhowany et
814 al. 2018).

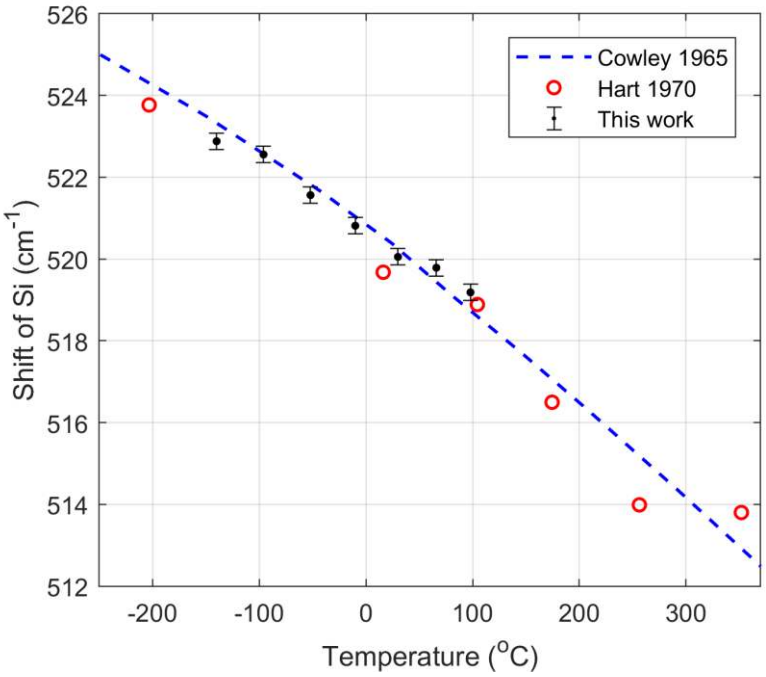

Fig. 8. Raman shift as a function of temperature for silicon to verify the thermal setup in the experiment. The blue curve is based on calculations from Cowley (1965). The red circles are based on experimental measurements in Hart et al. (1970). In this study, the error bar for spectral shift is ca. 0.2cm^{-1}.

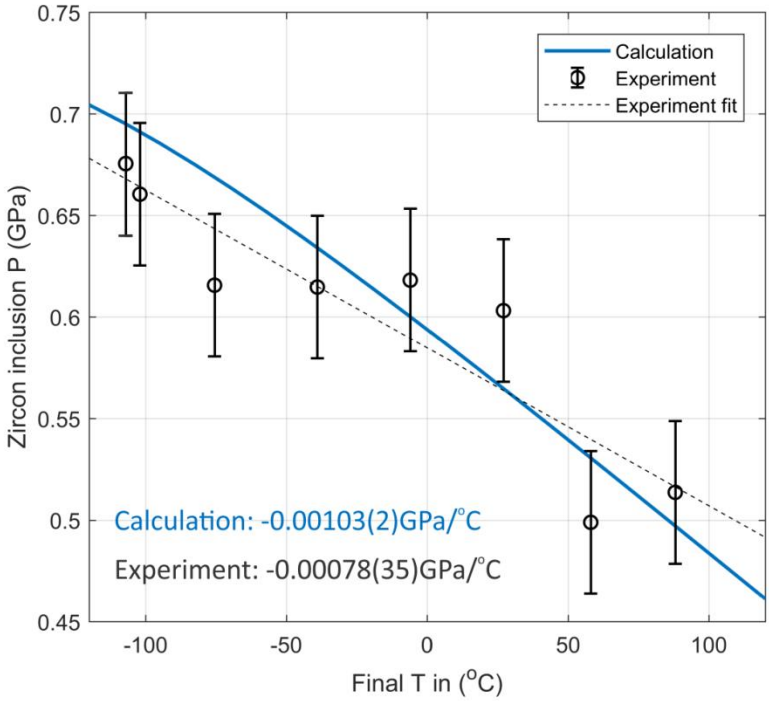

Fig. 9. Residual zircon pressure as a function of controlled temperature on the stage. The residual pressure is computed using the measured Raman shift of 1008cm^{-1} band subtracted by the influence of temperature on the same Raman band (Schmidt et al. 2013). The blue curve is computed based on elastic model. The entrapment *P-T* condition is taken at 2GPa and 700°C. The fitted slopes of pressure with respect to final temperature based on calculation and experiment are shown in the figure. The garnet composition is $Alm_{0.45}Prp_{0.40}Grs_{0.14}Sps_{0.01}$.

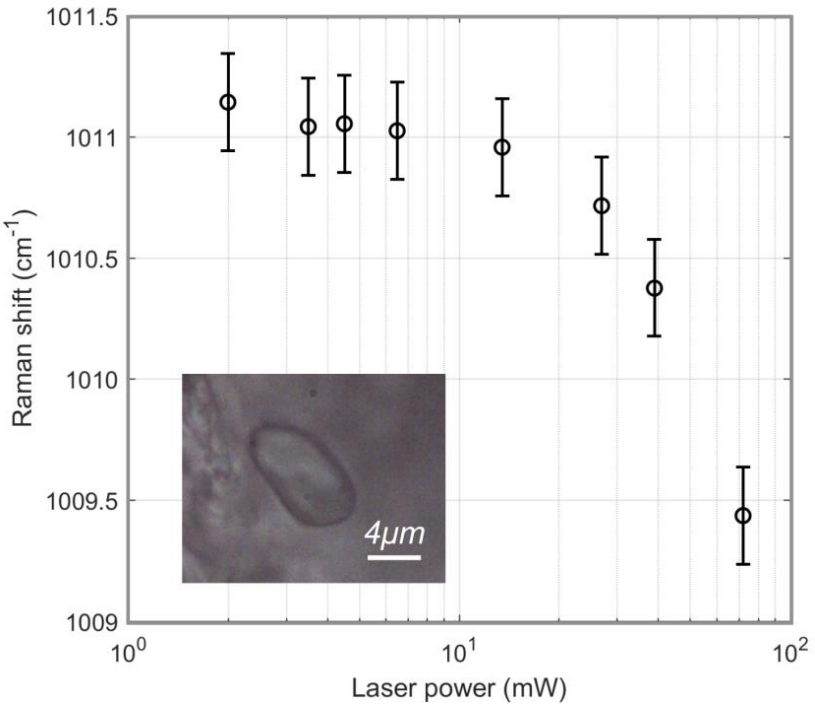

Fig. 10. Raman shift of a pressurized zircon inclusion as a function of applied laser power. The laser power is controlled by combining different filters (reduction of the incident laser power by 90%, 50% and 33%). No burning effect of the garnet and zircon has been observed (see the zircon inclusion after applying the maximal laser power). The residence time of the laser is ca. 30s. The Raman shift dramatically decreases when the laser power is higher than ca. 20mW, potentially due to the local heating at the focus point by the laser beam. A safe laser power is determined to be <10~20mW, where no significant variation of Raman shift is observed. In this study, we keep <5mW laser power with ca. 30s residence time.

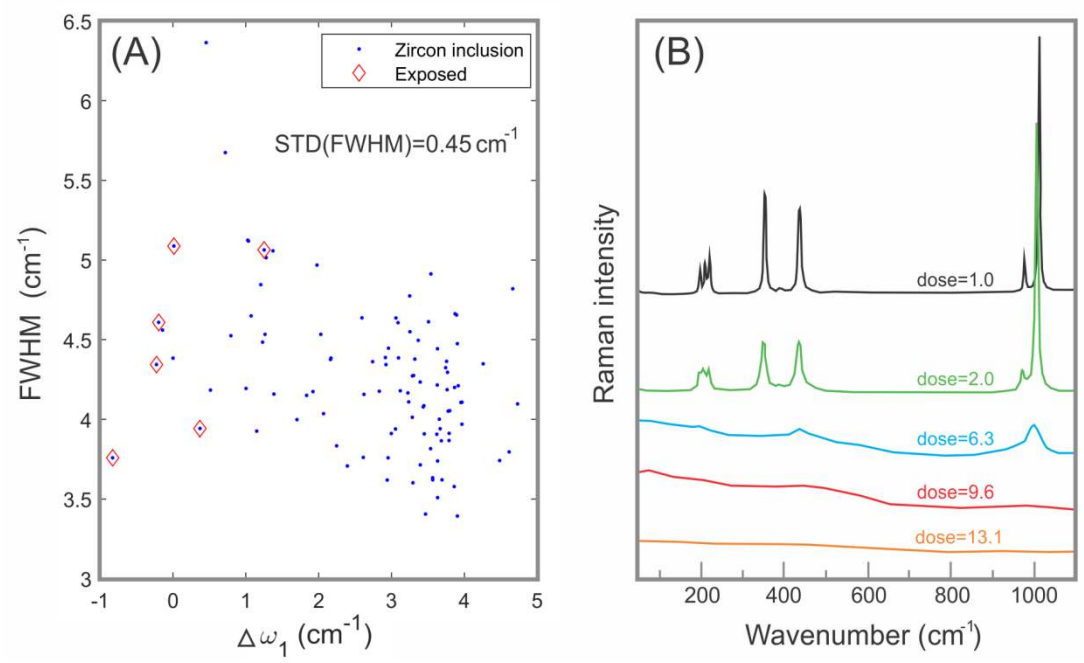

842

843 Fig. 11. (A) shows the full-width at half-maximum (FWHM) of 1008cm^{-1} peak with
844 respect to $\Delta\omega_1$. No clear relation can be observed between FWHM and $\Delta\omega_1$. The
845 FWHM for relaxed/exposed zircon inclusions is rather scattered and is averaged
846 slightly higher than highly pressurized zircons. Standard deviation of FWHM is ca.
847 0.45cm^{-1}. (B) shows the effect of radioactive decay on Raman spectra redrawn based
848 on data from the Figure 1 in Zhang et al. (2000). The dosage has unit 10^{18} α-event
849 per gram. It is shown that spectral broadening and spectral shift towards lower
850 wavenumber occur as radioactive dosage increases that causes structural damages.

851

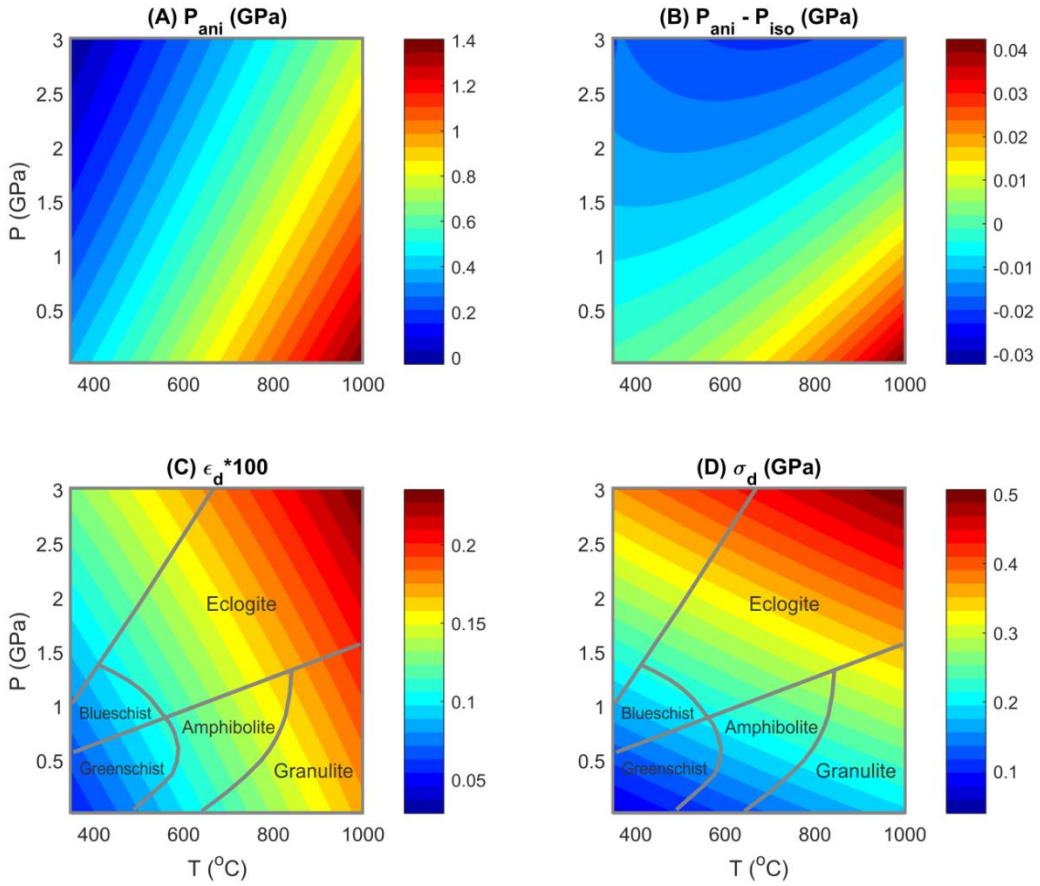

Fig. 12. (A) shows the residual zircon inclusion pressure in pyrope garnet host based on anisotropic model at different entrapment *P-T* conditions. The applied thermo-elastic constants are in Table 3. (B) shows the calculated residual pressure difference between anisotropic model and isotropic model. For isotropic model, only the volume is used following Eq. 3. For most geologically relevant *P-T* conditions, the difference of pressure between anisotropic and isotropic model is within 0.02GPa. (C) and (D) show differential strain and stress, respectively. It is shown that both residual strain and stress increase monotonically towards high entrapment *P-T* conditions.

TABLE

Table 1. Fitted parameters for the equation of state of isotropic zircon. The reference point is taken at room *P-T* conditions. Parameters are fitted using experimental measurements performed at room *P*, or room *T* individually. Linear $\frac{\partial K}{\partial T}$ model is used assuming constant $\frac{\partial K}{\partial T}$ value.

Model	V_0	K_0 (GPa)	K'	$\frac{\partial K}{\partial T}$ (GPa/°C)	$\alpha_{V0} \times 10^6$ (°C^{-1})	$\frac{\partial \alpha_V}{\partial T} \times 10^8$ (°C^{-2})
Linear $\frac{\partial K}{\partial T}$	260.89	199.0 [1]	4.0 [1]	-0.03 [2]	8.95 [3]	1.14 [3]

[1] Fitted using the experimental data of synthesized pure zircon in Van Westrenen et al. (2004).

[2] Obtained from the gradient of bulk modulus as a function temperature based on the *ab initio* calculations in Chiker et al. (2016).

[3] Fitted using the experimental data of natural zircon from Austin (1931). The fitted thermal expansion coefficient is similar in Subbarao and Gokhale (1968) and Özkan (2008).

875 Table 2. Raman shift measured in-situ as a function of controlled temperature on the
876 stage. Temperature is rounded to 0.5°C. The measured pressure is computed using the
877 measured Raman shift subtracted by the temperature contribution ω_T divided by
878 5.77cm^{-1}/GPa (Schmidt et al. 2013). The expected pressure is computed using
879 isotropic elastic model. Considering the uncertainty of Raman shift to be 0.2cm^{-1}, the
880 propagated uncertainty for pressure is ca. 0.035GPa.

Stage T	Measured shift	$\bar{\nu}_T$ (cm^{-1})	Measured P	Expected P
88.0	1009.16	1006.24	0.514	0.496
58.0	1010.01	1007.17	0.498	0.528
27.5	1011.54	1008.11	0.603	0.563
-6.0	1012.59	1009.07	0.618	0.600
-39.0	1013.50	1010.00	0.615	0.634
-75.5	1014.49	1010.98	0.616	0.669
-102.0	1015.43	1011.67	0.660	0.693
-107.0	1015.64	1011.79	0.675	0.696

881

882

883 Table 3. Thermo-elastic constants of zircon for investigating the effect of anisotropy
884 on residual stress and strain. The elastic constants are from Özkan and Jamieson
885 (1978), thermal expansion coefficients are averaged from Austin (1931). They are
886 assumed to be constant in *P-T* space for first-order approximation.

	C_{11}	C_{33}	C_{12}	C_{13}	C_{44}	C_{66}	α_1 (10^{-6})	α_3 (10^{-6})
Zircon	424.4	489.6	69.2	150.2	113.3	48.2	3.3	6.0

887

888 **APPENDIX**

889 **Eshelby's solution**

890 The Eshelby's analytical solution is briefly introduced here. Detailed explanations can
891 be found in Mura (1987). The Voigt notation and Einstein's summation are applied.
892 Constant elastic stiffness tensor at any *P-T* conditions is assumed here for simplicity
893 (not necessarily for the Eshelby's solution). The residual inclusion strains after
894 exhumation from entrapment *P-T* conditions can be described by the following
895 equation:

$$\varepsilon_i = \mathbb{s}_{ij} e_j^* - e_j \tag{A1}$$

896 where ε_i are the residual strains of inclusion, e_j are the eigenstrains, e_j^* are the
897 equivalent eigenstrains, and $\mathbb{s}_{ij}$ denote the Eshelby's tensor defined as follows for a
898 spherical inclusion (Mura 1987):

$$\begin{aligned} &\mathbb{s}_{11} = \mathbb{s}_{22} = \mathbb{s}_{33} = \frac{7-5\nu}{15(1-\nu)} \\ &\mathbb{s}_{12} = \mathbb{s}_{21} = \mathbb{s}_{23} = \mathbb{s}_{32} = \mathbb{s}_{13} = \mathbb{s}_{31} = \frac{5\nu-1}{15(1-\nu)} \\ &\mathbb{s}_{44} = \mathbb{s}_{55} = \mathbb{s}_{66} = \frac{4-5\nu}{15(1-\nu)} \end{aligned} \tag{A2}$$

899 where ν is the garnet host's Poisson ratio. The other components of $\mathbb{s}_{ij}$ are zero. The
900 equivalent eigenstrains are defined as follow:

$$e^* = [C - (C - \bar{C})\mathbb{s}]^{-1}\bar{C}e \tag{A3}$$

901 where $\bar{C}$ and C are the inclusion and host's stiffness tensor, respectively. The
902 eigenstrains e_j characterize the difference of thermo-elastic deformation between the

inclusion and host in response to the changes of confining pressure and temperature. They are defined as:

$$e_1 = -(\varepsilon_1^{zr} - \varepsilon^{grt}) \tag{A4}$$

$$e_3 = -(\varepsilon_3^{zr} - \varepsilon^{grt})$$

where ε_1^{zr} and ε_3^{zr} are the zircon strain components defined at entrapment *P-T* conditions. The reference state (strain-free) is defined at room *P-T* conditions. For garnet, the strains are isotropic and denoted by ε^{grt} at entrapment *P-T* conditions.

Given anisotropic stiffness tensor and thermal expansion coefficient of the zircon inclusion (see Table 3), ε_1^{zr} and ε_3^{zr} can be computed at any *P-T* conditions and substituted into A4. Given eigenstrains e_j, it is possible to compute the equivalent eigenstrain defined in A3. Finally, the equivalent eigenstrains e_j^*, eigenstrains e_j and Eshelby's tensor $\mathbb{s}_{ij}$ are all substituted into A1 to compute the residual inclusion strain after exhumation. The residual inclusion stresses are expressed as below using the inclusion's stiffness tensor $\bar{C}_{ij}$:

$$\sigma_i = \bar{C}_{ij}\varepsilon_j \tag{A5}$$